

See discussions, stats, and author profiles for this publication at: <https://www.researchgate.net/publication/231369812>

Flow Mapping and Modeling of Liquid–Solid Risers

ARTICLE *in* INDUSTRIAL & ENGINEERING CHEMISTRY RESEARCH · AUGUST 2001

Impact Factor: 2.59 · DOI: 10.1021/ie010181t

CITATIONS

42

READS

29

2 AUTHORS:



Shantanu Roy

Indian Institute of Technology Delhi

81 PUBLICATIONS **717** CITATIONS

SEE PROFILE



Milorad Duduković

Washington University in St. Louis

315 PUBLICATIONS **7,118** CITATIONS

SEE PROFILE

Flow Mapping and Modeling of Liquid–Solid Risers

Shantanu Roy[†] and M. P. Dudukovic*

Chemical Reaction Engineering Laboratory, Department of Chemical Engineering, Washington University, One Brookings Drive, St. Louis, Missouri 63130-4899

The trend toward environmentally benign processing has resulted in novel chemistries and new reactor types. For alkylation of both aromatics and linear paraffins, with new solid acid catalysts, liquid–solid risers are one of the reactor types considered. As the fluid dynamics of liquid–solid risers is largely unknown, it has been investigated in this work in a 6-in.- (15-cm-) diameter “cold-flow” circulating fluidized-bed riser using noninvasive methods. The time-averaged solids holdup distribution is determined by γ -ray computed tomography (CT). The solids instantaneous and ensemble-averaged velocity patterns, as well as the solids residence time distribution in the riser, is obtained by computer-automated particle tracking (CARPT). Various measures of solids backmixing are evaluated including the eddy diffusivities and the overall axial dispersion coefficient. The obtained database is used for validation of a two-fluid Euler–Lagrange model, which is coupled with appropriate closures including the kinetic theory of granular solids. The model is shown to be capable of predicting the liquid and solids residence time distributions in the riser as well as the solids velocity and holdup pattern. The quantitative predictions from the two-dimensional axisymmetric simulation for the solids volume fraction and the time-averaged solids axial velocity radial distributions agree well with the experimental data. The model can be used to predict the extent of solids backmixing in the reactor.

1. Introduction

Multiphase reactors are prevalent in the chemical, petroleum, and associated process industries. Proper reactor selection determines the features and costs of the whole plant. Environmental considerations play an ever-increasing role in the selection of process chemistry, which, in turn, must be matched by an appropriate reactor type. The old-fashioned approach of conducting the reaction on a multitude of reactor scales on the way to commercialization is increasingly replaced by a more systematic systems approach. In this approach, one attempts to develop reactor models that elucidate the key features of the multiphase flow pattern, measure the relevant physical quantities, and model them with suitable accuracy. Only with well-understood flow field information can an accurate kinetic model describing the reaction chemistry produce meaningful predictions of reactor performance.^{1–4} The current public expectations of clean, safe, environmentally acceptable processes leads us to novel chemistries and reactors. For example, the push to replace liquid catalysts, such as HF and sulfuric acid in alkylation processes, has resulted in the development of solid acid catalysts, which, in turn, require novel multiphase reactors, such as liquid–solid circulating fluidized beds. In this contribution, we consider and study the fluid dynamics of the riser in a liquid–solid circulating fluidized-bed system.

Liquid–solid circulating reactors form the heart of emerging alkylation processes for the production of motor fuel additives and also for the manufacture of linear alkylbenzene (LAB).^{5,6} The mandated use of

reformulated gasoline (RFG) in North America and the increasingly stringent gasoline standards being enacted around the world have led to a surge in demand for motor fuel alkylate (which is an ideal gasoline additive with a low Reid vapor pressure; high octane number; and low content of aromatics, sulfur, and olefins). On the other hand, linear alkylbenzene (typically manufactured by the alkylation of benzene) is the single most widely used component of industrial and household detergents and has experienced an average of 4–5% annual growth rate in worldwide demand in the past decade.⁷

Alkylation processes have been and continue to be a very important class of industrial reactions. Conventionally, the manufacture of LAB and other alkylated olefins and aromatics have been effected through the use of strong liquid acids (homogeneous catalysts), such as hydrofluoric acid (HF) and sulfuric acid (H₂SO₄).^{5,6,8,9} There are, however, several problems with the existing technologies. Most important among these are the use of corrosive acids, equipment corrosion, hazards to operating personnel, and environmental threats posed by both strong liquid-phase acids and undesirable byproducts. Typically, in these liquid acid-catalyzed processes, the reactor turnover times are on the order of 20–30 min.

The aim of making alkylation more environmentally benign and also of improving process selectivity and productivity resulted during the past decade in the emergence of solid-phase acid catalysts and of liquid–solid circulating fluidized beds as the reactors of choice. Liquid–solid riser technology became possible because of the development of solid acid catalysts, specifically, either zeolites with acidic properties (e.g., zeolite/BF₃),^{5,10} or solid superacids in inorganic and organic supports.⁵ Although these catalyst chemistries produce better selectivities and yields of the desired product, with mean catalyst residence times for optimal conver-

* Author to whom all correspondence should be addressed. Phone: (314) 935 6021. Fax: (314) 935 4832. E-mail: duduk@poly1.che.wustl.edu.

[†] Present Address: Corning Incorporated, Process and Product Modeling, SP DV 01 MOD 6, Corning, NY 14831.

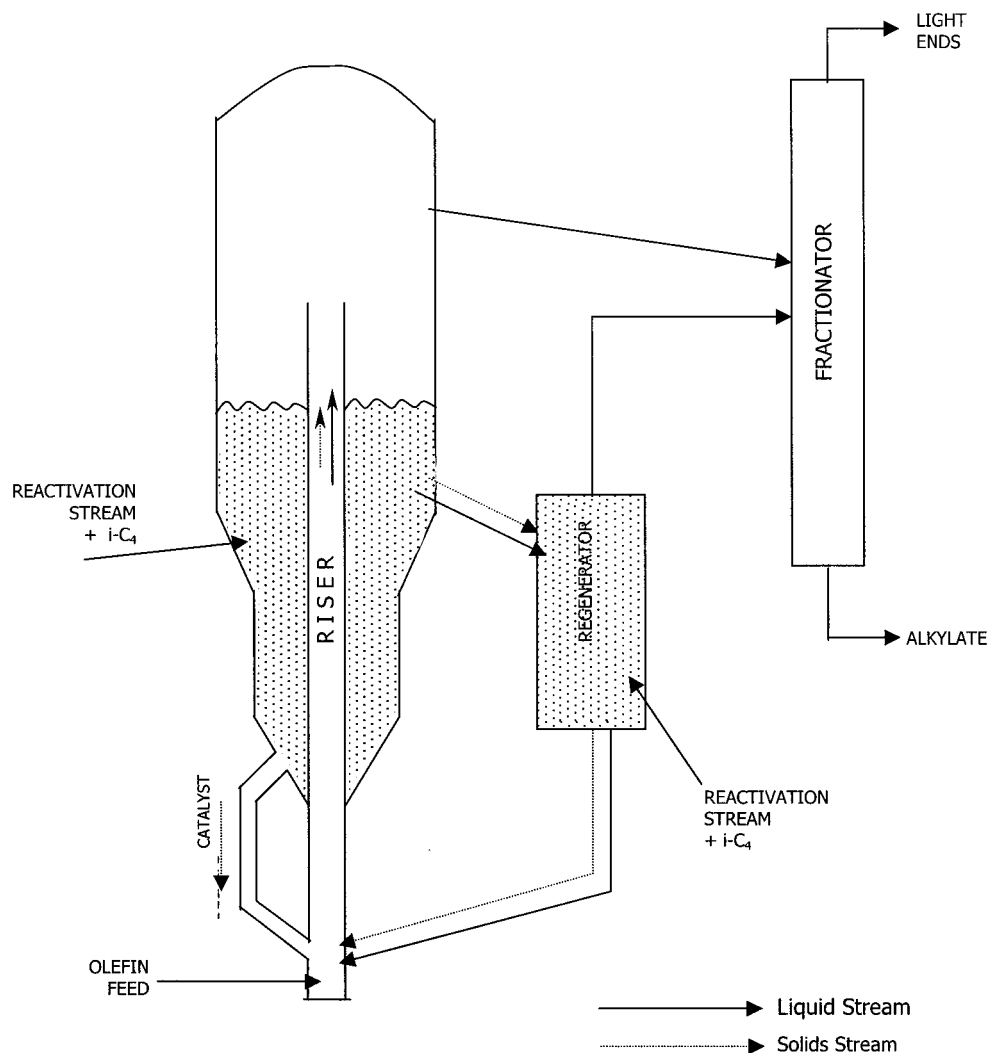


Figure 1. Schematic diagram of the liquid–solid circulating fluidized-bed process for alkylation.

sion of around a minute, the solid catalyst is deactivated rapidly and needs to be periodically recycled to ensure continuous operation. It therefore seems natural that a favorable liquid–solid contacting configuration for a process that uses solid acid catalysts for aromatic and olefin alkylation is a liquid–solid circulating fluidized bed, in which the continuous phase consists of the liquid-phase hydrocarbons at high pressure and low temperature and the dispersed phase is the solid catalyst (http://www.uop.com/home/refining/processes_and_products/alkylene_intro.htm). The alkylation reaction is effected in a riser vessel, in which the solids and the liquid phase flow cocurrently upward, such that the deactivated catalyst exits the riser along with the liquid-phase product stream. A solid–liquid separator separates the two phases external to the riser. The liquid stream is sent for downstream processing, while the solid acid catalyst is regenerated and recycled back into the riser vessel along with the fresh or recycled (unreacted) liquid feed. Figure 1 shows a simplified schematic of the process flow sheet. The principal alkylation reaction occurs in the riser, and the liquid-phase products are subsequently separated, while the solids are recycled back into the riser after regeneration. This process technology is environmentally benign and safe for operating personnel, and it replaces the earlier technology that relied on liquid-phase hydrofluoric or

sulfuric acid as catalyst, both of which are hazardous chemicals to the environment.

Naturally, because the reaction kinetics is relatively fast and the process is continuous with high throughput rates, the critical features determining the process efficiency are the mode of liquid–solid contacting and the extent of backmixing of the phases in the riser (where the desired reaction is performed). These factors are particularly important because the overall process chemistry can be approximately represented by two parallel reactions. The main desired second-order reaction is first-order in olefin and paraffin, while the undesired side reaction, the extent of which is proportional to catalyst deactivation, is second-order in olefin concentration. The ability to predict the extent of backmixing and the quality of liquid–solid contacting calls for an understanding and quantification of the fluid dynamics and flow patterns. The objectives and emphasis of this work were to provide such a quantification of the liquid–solids flow pattern and to develop the means for predicting the extent of backmixing with process scale-up.

Very little is known about the solids flow pattern in a liquid–solid riser (as opposed to the extensive knowledge of gas–solid risers). It is expected that these flow patterns are highly turbulent and chaotic and that they certainly contain a high volume fraction of solids.

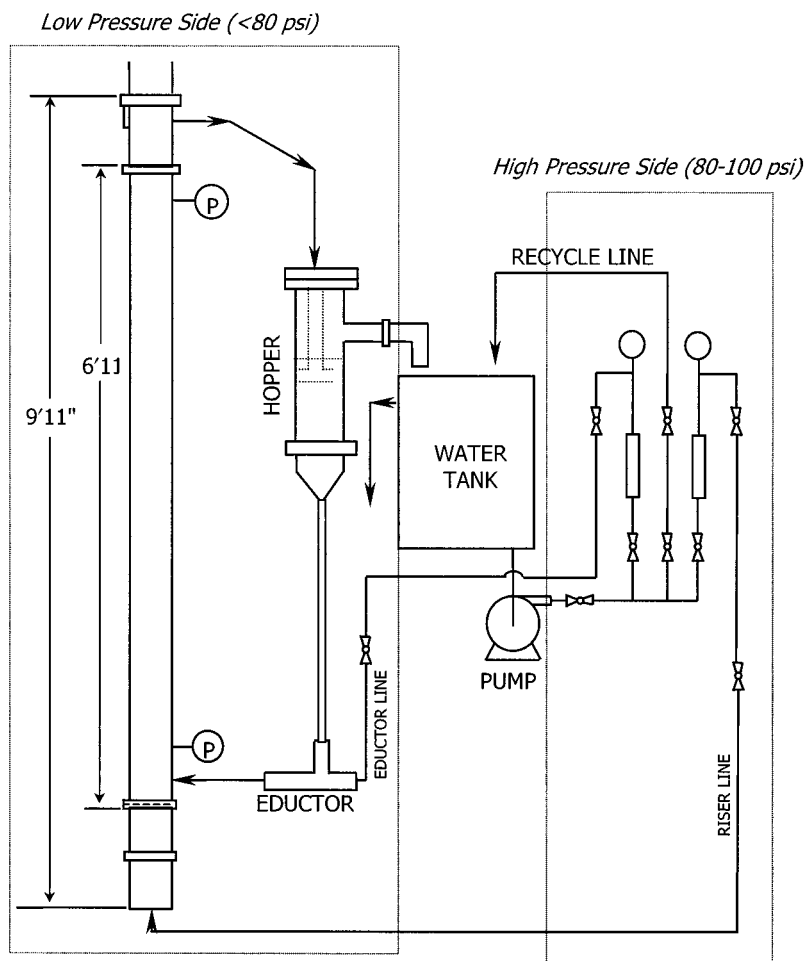


Figure 2. Schematic diagram of laboratory-scale liquid–solid circulating fluidized-bed setup for cold flow experiments on the riser.

Noninvasive experimental measurements are performed to identify the solids volume fraction profiles in the riser, the solids velocity patterns, and the mixing patterns. These data are then used for validation of a k -fluid model implemented with appropriate closure schemes. The main objective of the study is to provide quality data for validation of the CFD model and to establish the model reliability for scale-up and design.

2. Experimental Studies

To study the fluid dynamics and the flow patterns that exist in a liquid–solid riser, a cold-flow mock-up unit was installed. The experiments were conducted with 2.5-mm glass beads with a particle density of 2.5 g/cm³ (total inventory of about 110 lb) as the solids phase and ordinary tap water as the liquid phase. A schematic diagram of the experimental unit is shown in Figure 2. The setup consists of a vertical 6-in.-i.d. Plexiglas column with a total height of about 10 ft, a 7-ft section of which represents the developed flow in the riser section. The riser has two inlet lines, one entering vertically below the 7-ft section (called the “riser line” in Figure 2), and the other entering horizontally a little above the distributor (called the “eductor line”). The solids (glass beads) enter the riser from the latter line, driven by the liquid phase (water), while the vertical line feeds the remaining water to the riser. The solids and liquid flow cocurrently upward in the riser and exit through a specially constructed frustum. An exit line conveys the liquid–solid mixture from the

head of the riser to the hopper, which maintains the inventory of the solids. In the hopper, a wire mesh separates the solids and the liquid. The liquid (water) is conveyed back into the holding water tank, while the solids pass through the vertical pipe below the hopper into the solids eductor. The total water flow rate to the system is maintained using rotameters positioned in both the riser and the eductor lines (Figure 2). The system was designed to operate in a “variable inventory mode”, i.e., the liquid and the solids flow rates can be controlled independently. The total liquid flow rate immediately downstream of the pump is split into three lines. Some of the liquid is used to direct all of the solids flow through the eductor line, while another portion flows through the riser line. A recycle line (Figure 2) was installed to return the excess liquid to the holding tank. This ensures a steady pressure head at the eductor and riser inlets and stable operation of the loop. The whole system is run at a pressure of 75 psig at the inlet to the riser.

Although the liquid flow rate through the riser could easily be controlled with the rotameters, it was essential to calibrate the eductor. This was accomplished using an independent experiment designed specifically for this purpose. The method was based on radioactive particle tracking and allowed us to accurately measure the solids flow rate as a function of eductor line liquid flow rate in situ and noninvasively. Details of these experiments have been discussed by Roy⁷ and by Roy et al.¹¹

Experiments were conducted at three liquid superficial velocities, (15, 20, and 23 cm/s) and at three solid-

to-liquid flow ratios of 0.10, 0.15 and 0.20 at each liquid flow rate. The overall solids holdup in the riser was estimated to be between 20 and 40% under these conditions. The extent of liquid backmixing was established by tracer methods. A saturated solution of potassium chloride (KCl) was injected as a pulse under pressure before the entrance of the riser, and the local conductivity of the liquid phase was sampled using strategically positioned conductivity probes at the entrance and exit of the riser. The moments of the tracer impulse response within the riser were evaluated.⁷ Liquid was found to be essentially in plug flow, as the dimensionless variance of the impulse response was always below 0.1. Thus, the liquid-phase dispersion was found to be quite low under all conditions studied.

We focused our attention on quantification of the flow pattern of the solid phase via determination of the radial solids holdup profiles, the solids ensemble-averaged velocity profiles, and the solids eddy diffusivities. For brevity, we present the results here only for a single liquid flow rate. A complete set of results is available in the D.Sc. thesis by Roy.⁷

2.1. Solids Volume Fraction Profile Measurements. The next phase of the experimental program involved the use of computer tomography (CT) in estimating the time-averaged solids volume fraction. For this work, the CT scanner developed in-house in CREL^{12,13} was employed, and the riser (in full operation) was positioned concentric to the scanner assembly. In γ -ray tomography, highly collimated and intense γ radiation is made to penetrate through the vessel of interest, and the attenuation (reduction in intensity) that the object causes is measured. The attenuation is a function of system density, and for a two-phase system, it is a measure of the phase holdup (volume fraction) that the radiation “sees” as it travels through the system. Many attenuation measurements are made in a horizontal plane around the column, and these sets of “projection measurements” are assembled and used to back-calculate the “image”, i.e., the spatial distribution of the two phases in the system. The details of the mathematical treatment for data acquisition and image reconstruction have been discussed by Kumar,¹² Kumar et al.,¹³ and Roy.⁷

CT scans at all liquid superficial velocities studied reveal relatively uniform solids holdups in any cross section of the riser with much less radial variation than experienced in gas–solid risers. Moreover, the holdup distributions are approximately axisymmetric under all conditions studied. Azimuthal averaging leads to radial solids holdup profiles, such as those shown in Figure 3 for three elevations and for three S/L ratios at the liquid superficial velocity of 20 cm/s. Figure 3 indicates that there is no significant axial gradient in the solids holdup among the levels at which the scans were performed, even though the level of 50 cm does seem to show a marginally greater solids volume fraction than the other two levels. In a time-averaged sense, the flow field seems to be developed independent of axial location in the region of 50–150 cm in the riser. There is a minor segregation of solids at the walls that seems to increase with increasing solids-to-liquid feed ratio.

The radial solids holdup profile at each operating condition can be represented well by eq 1

$$\epsilon_s(r) = \frac{(m+2)}{\epsilon_s(m+2+2c)} \left[1 + c \left(\frac{r}{R} \right)^m \right] \quad (1)$$

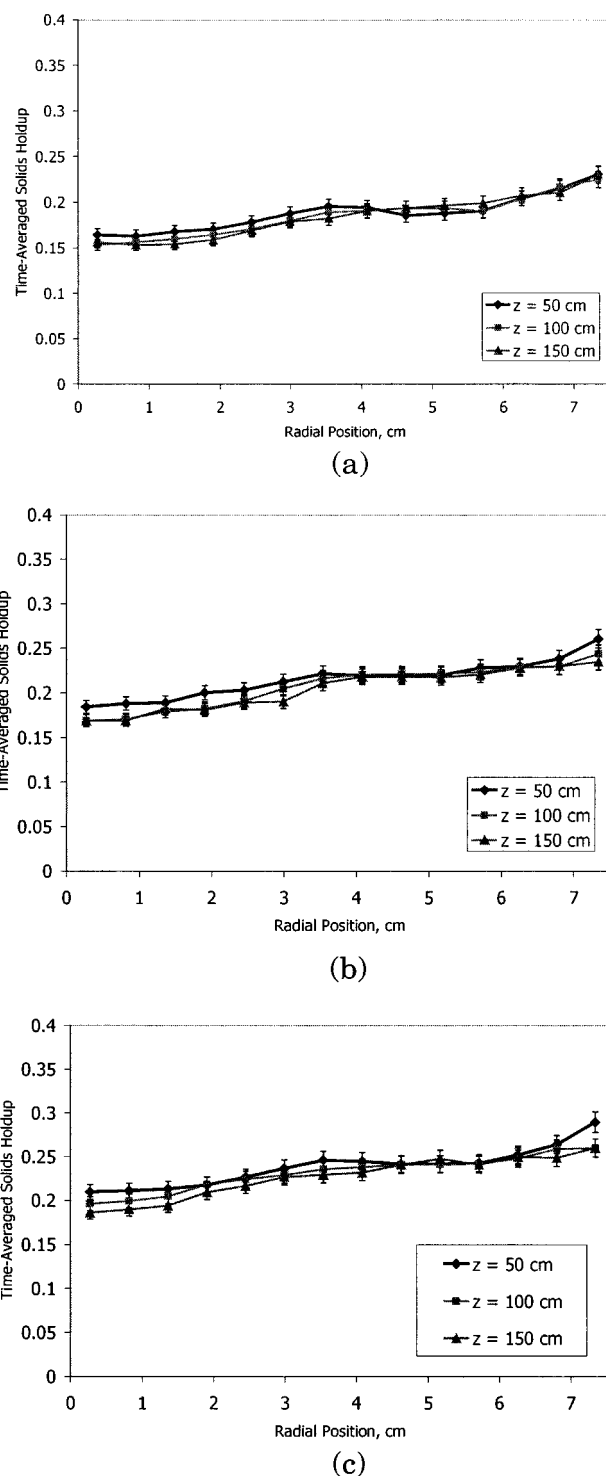


Figure 3. Circumferentially averaged time-averaged solids holdup distribution in the liquid–solid riser at $U_L = 20$ cm/s. (a) $S/L = 0.10$, (b) $S/L = 0.15$, (c) $S/L = 0.20$.

Pertinent parameters for different solids-to-liquid flow ratio at $U_L = 20$ cm/s are shown in Table 1, while the results for all operating conditions studied are provided by Roy.⁷ One observes that increasing the solids-to-liquid flow ratio at fixed liquid superficial velocity increases the average solids holdup (Table 1), whereas increasing the liquid superficial velocity at fixed liquid–solids flow ratio decreases the overall solids holdup somewhat.⁷

2.2. Solids Velocity Field Measurements. Measuring the solids velocity field and the solids backmixing

Table 1. Parameters for Solids Holdup and Solids Average Axial Velocity Profiles^a

S/L (solids/ liquid flow ratio)	$\bar{\epsilon}_s$ (mean solids holdup)	m (for eq 1)	c (for eq 1)	$V_z(0)$ (cm/s eq 2)	α_1 (cm/s eq 2)	α_2 (cm/s eq 2)	n (eq 2)
0.10	0.19	1.22	0.44	12.8	5187	5202	3.21
0.15	0.21	0.78	0.47	14.2	3508	3525	3.33
0.20	0.23	0.75	0.39	16.0	5654	5674	3.29

^a Liquid superficial velocity $U_L = 20$ cm/s.

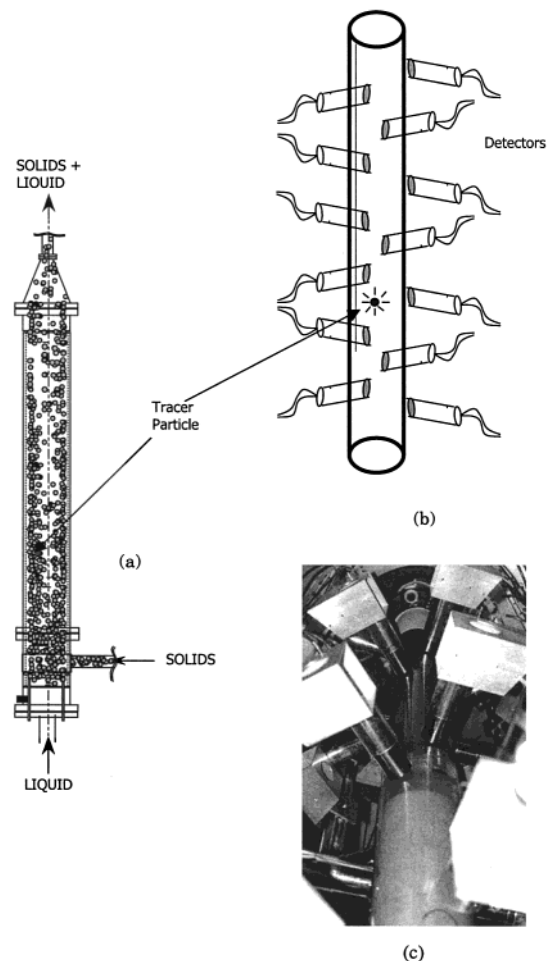


Figure 4. Schematic diagram of CARPT configuration around the liquid-solids riser. (a) Riser with solids inventory and tracer particle indicated. (b) Detectors sensitive to tracer particle location, positioned around column at strategic locations. (c) Perspective view of the CARPT installation around the liquid-solids riser.

is not trivial in a system such as the liquid-solids riser. The natural opacity of the system renders the use of optical techniques impractical even for velocity measurements at the wall, and intrusive probes for sampling solids and measuring their free stream velocity cannot be used because of the highly turbulent flows that exist inside. Thus, computer-automated radioactive particle tracking (CARPT) was employed to determine the solids velocities in a noninvasive manner. This technique has been successfully implemented on multiphase reactors such as bubble columns and three-phase fluidized beds (see, e.g., refs 14–16) and was suitably tailored for the present setup. Figure 4a and b displays a schematic representation of the CARPT technique as implemented on the liquid-solids riser, while Figure 4c presents a close-up photograph of the CARPT detector configuration.

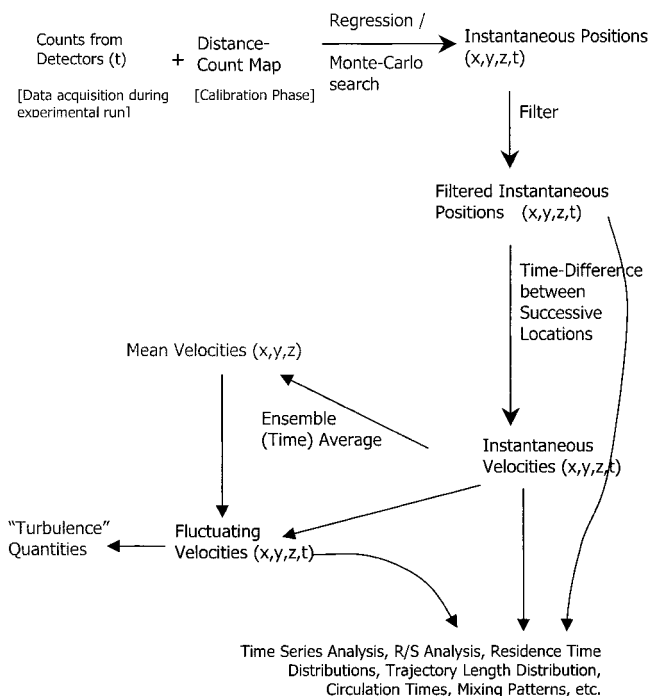


Figure 5. Flowchart for CARPT data acquisition and processing.

In CARPT, the motion of a single radioactive tracer particle is mapped out. For tracing the solids in the liquid-solids riser, a tracer particle was designed by encapsulating radioactive Sc-46 (which emits γ radiation) with an air gap in a small steel spherical shell. The tracer was of exactly the same dimensions as the particles in the solids inventory and had the same effective density as the solid particles. With the system in operation, the tracer particle is allowed to move freely, and being hydrodynamically similar to the particles in the solids inventory, it mimics the behavior of the rest of the solid particles. Strategically placed scintillation detectors measure the photon counts emitted by the tracer particle. This process is completely automated, and the data are acquired at high enough frequency (50 Hz) that successive instantaneous positions of the particle are recovered with fidelity. By collecting statistically significant data, it is possible to extract the ensemble-averaged velocity fields and mixing patterns of the traced phase in opaque systems. The details of the position and velocity reconstruction have been discussed in Roy.⁷ Figure 5 shows a flowchart of the data-processing protocol.

As the tracer particle moves in the circulating fluidized-bed loop, it periodically passes through the zone of interrogation of the detectors in the riser (Figure 4c). The detector positioned at the entrance to the riser signals the arrival of the tracer particle, which triggers the data acquisition system to start acquiring the counts from all of the detectors located around the riser. Data acquisition continues until the detector located at the top of the riser signals that the tracer particle has passed it on its way out of the riser. This kind of data acquisition protocol is unique to a circulating system such as the one studied and, in this respect, is different from that used in earlier works.^{14–16} The time that elapses between the signals at the exit detector and at the entry detector is the sojourn (residence) time of the tracer in the riser during that particular visit. The detectors around the riser record the tracer position

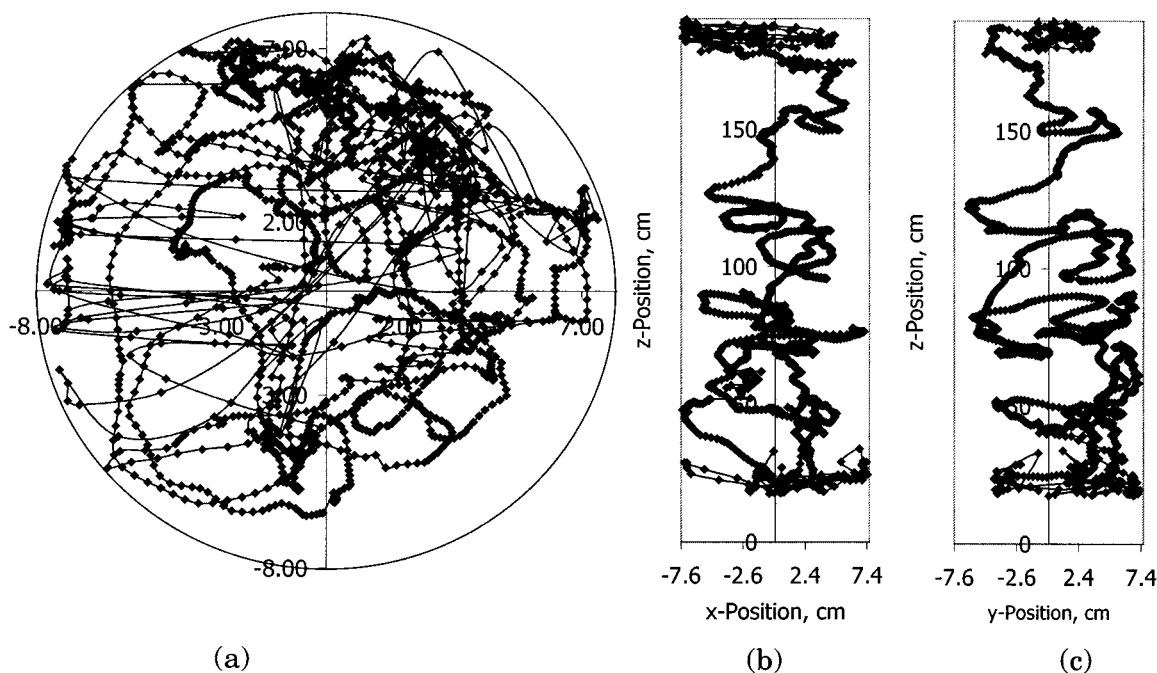


Figure 6. Single trajectory of tracer particle ($U_L = 20$ cm/s, $S/L = 0.15$) during a residence time of 38 s (1900 successive positions) in the column. (a) x - y plane, (b) x - z plane, (c) y - z plane.

during its sojourn through the riser. Figure 6 describes one such typical tracer trajectory during a single tracer sojourn through the riser that spanned over 38 s and, hence, a trace of 1900 consecutive positions (data acquired at a sampling frequency of 50 Hz). Figure 6a shows the tracer trajectory projection on the horizontal (x - y) plane, while Figure 9b and c shows the projections on the x - z and y - z planes, respectively. Clearly, the tracer particle follows a tortuous path, sometimes accelerating and sometimes decelerating, as indicated by the fact that the separation between successive locations (at constant time intervals) is not constant. By time-differencing the successive positions of the tracer particle, one recovers the instantaneous particle velocity at any given location in the riser. The probability density functions (histograms) of instantaneous velocity components of the tracer particle at various axial and radial levels can be and have been constructed.⁷ Each of the three velocity components has a unimodal distribution with a well-defined mean (close to zero for the radial and azimuthal components and a finite positive or negative value for the axial component, depending on the radial location). Invoking the ergodic hypothesis, we assert that these probability density functions, which are truly generated by "ensemble sampling" of the Lagrangian particle trace at any location, are identical to the statistics of time variation of the instantaneous velocity of the solids phase (which the tracer particle is designed to trace) at any given location in the column.

Repeated tracer trajectories confirm the general features observed in Figure 6 that the tracer particle, and hence the solid particles in general, experiences significant velocity fluctuations (from -25 to $+25$ cm/s) and rarely rises vertically upward in a straight line. Typically, it follows a tortuous path indicative of turbulent flow. Indeed, this conclusion is also borne out by visual observation of the liquid-solid riser operation, which is highly turbulent and chaotic and characterized by large-scale vortical structures that sweep the particles. The question we wish to address is: What does

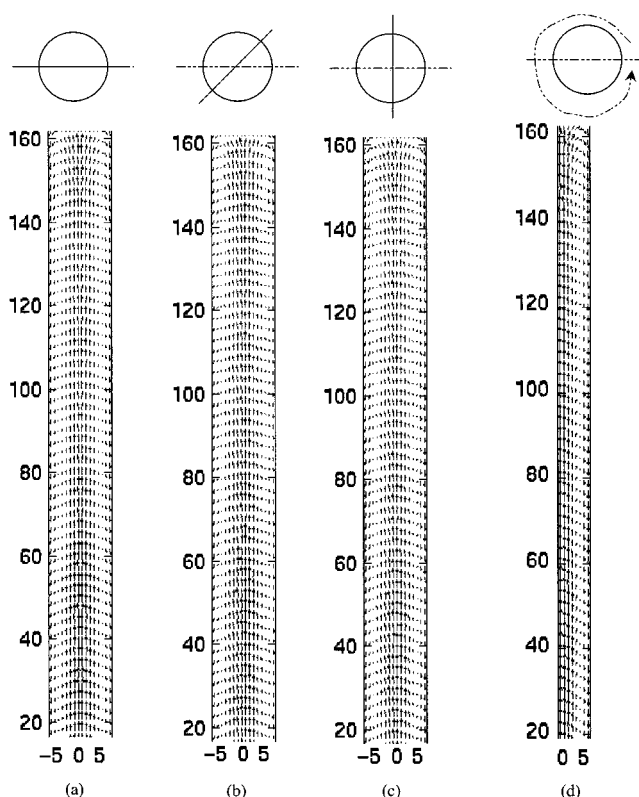


Figure 7. Solids velocity vector plots at $U_L = 23$ cm/s and $S/L = 0.10$: (a) in a typical r - z plane, (b) at 45° to the first plane, (c) at 90° to first plane. (d) Flow field has been azimuthally averaged (0 - 360°) to yield an axisymmetric velocity vector plot. (Vectors have been interpolated between planes to yield a more uniform vector plot. Longest vector represents a velocity of 20 cm/s.)

the motion of the solids phase *as a whole* look like? The answer is provided by Figure 7, which is a vector plot of the time-averaged solids velocity ($U_L = 23$ cm/s, $S/L = 0.10$), generated by finding the mean of the probability densities for the solids velocities at each location in the column. In Figure 7a-c, the projections of the solids

ensemble-averaged velocity vectors are plotted in three different r - z planes, each separated by 45° . Clearly, the solids velocity vectors point upward at the center of the column and downward at the wall. Also, visually, the flow field appears axisymmetric (i.e., independent of θ), indicating that the *mean* radial and azimuthal components of velocity are very small. In Figure 7d, the azimuthally averaged solids velocity vectors are plotted. Thus, even though the solid-phase particles (represented by the tracer particle) take tortuous paths in their sojourn from the inlet to the exit of the riser (Figure 6), the time-averaged picture (constructed with data collected over 40 h) is ordered and has a clear pattern (Figure 7).

The azimuthally averaged solids velocity can be plotted as a function of radial position. A typical plot is shown in Figure 8, where one observes that the solids flow above 50 cm is fully developed in the time-averaged sense and that no significant variation in the radial profile of the axial component of solids velocity can be observed. At all the conditions studied, there is always an annulus of solids at the wall that is flowing down in a time-averaged sense. The solids velocity profile is a roughly cubic function of radial location, the highest velocity being at the center of the column and the velocity being negative near the wall. The exact location of the "crossover" (i.e., the location at which the profile crosses the abscissa) does not appear to exhibit any trend. The downflow of solids at the wall (seen both in Figures 7 and 8) is expected to cause considerable backmixing in the solid phase. Because the solids holdup is higher at the wall as compared to the center of the column, the annulus of negative velocities at the wall makes for significant downward mass flow of solids in the column.

From an engineering perspective, it is useful to develop a correlation for the radial variation of the axially averaged solids velocity profile. An expression that has been found to describe the radial profile of the axial solids velocity satisfactorily is

$$v_z(r) = v_z(0) + \alpha_1 \left(\frac{r}{R}\right)^n - \alpha_2 \left(\frac{r}{R}\right)^{n\alpha_1/\alpha_2} \quad (2)$$

In eq 2 above, $v_z(0)$ is the centerline axial solids velocity, and α_1 and α_2 are empirical constants determined by curve fitting. The exponent n defines the curvature of the velocity profile. The pertinent parameters for the operating conditions studied are provided by Roy,⁷ and the parameters at $U_L = 20$ cm/s are shown in Table 1.

Because the eductor was calibrated independently of the CARPT-CT measurements, we compare the total solids flow rate in the riser determined by the eductor, Q_{se} , with the flow rate estimated by eq 3 ($\langle Q_s \rangle$), which utilizes the ensemble-averaged axial solids velocity profile, $\langle v_z(r) \rangle$ as determined by CARPT and the time-averaged solids holdup profile $\langle \epsilon(r) \rangle$ as determined by CT.

$$\langle Q_s \rangle \approx 2\pi \int_0^{R_i} r \langle \epsilon_s(r) \rangle \langle v_z(r) \rangle dr \quad (3)$$

The relative error $[(Q_{se} - \langle Q_s \rangle / Q_{se})] \times 100$ is always negative and lies within -5 and -10% .⁷ This could indicate that the integral of the cross-correlation term $\langle \epsilon'(r) v_z(r) \rangle$, which is neglected in eq 3, is small but always positive. Because the CT-determined solids holdup profile and the CARPT-determined solids veloc-

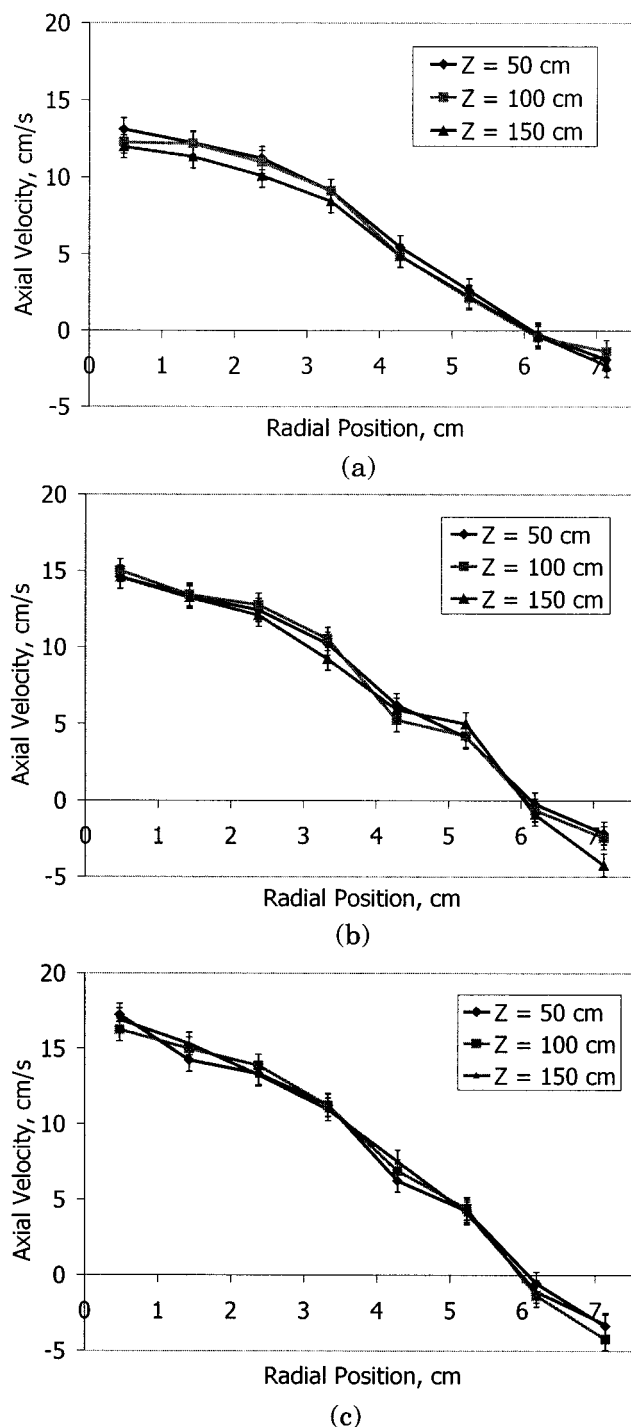


Figure 8. Azimuthally averaged time-averaged axial solids velocity profiles as functions of radial and axial position at a liquid superficial velocity of 20 cm/s. (a) $S/L = 0.10$, (b) $S/L = 0.15$, (c) $S/L = 0.20$.

ity profile lead to reliable estimates of the total solids flow rate, we use these quantities also to estimate the upflow solids flow rate (in the region $0 < r < r_f$) and the downflow solids flow rate (in the region $r > r_f$). The percentage of solids in downflow varies from 7 to 16%. The downflow at fixed liquid superficial velocity increases with solids-to-liquid flow ratio and increases with liquid velocity at fixed liquid-to-solids flow ratio. This seems to suggest that enhanced solids downflow should result in enhanced solids backmixing, which is increased under conditions that favor an increase in flow rates and randomness in the system.

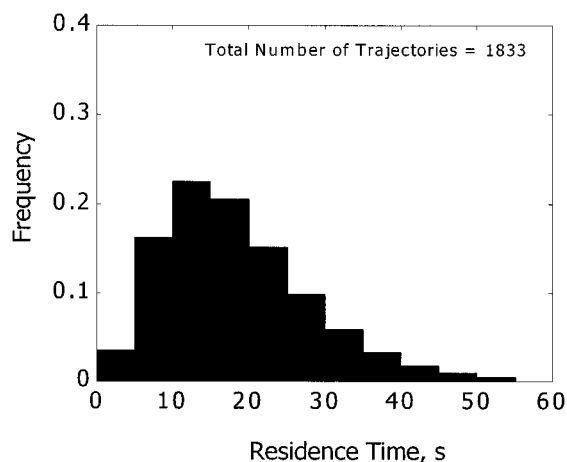


Figure 9. Typical residence time distributions calculated from CARPT data. ($U_L = 20$ cm/s; $S/L = 0.10$).

2.3. Solids Backmixing. The CARPT results provide us with a rich source of information regarding local probability density functions of solids velocity components. From this information on instantaneous velocities, *in addition* to the mean velocity fields, one is able to recover the kinetic energy of fluctuations, rms velocities, rescaled-range (Hurst) coefficients, trajectory length distributions, return length distributions, circulation time distributions, and a whole range of other “hydrodynamic goodies”, details of which are reported by Roy.⁷ However, here we discuss only the usual measures of backmixing typically employed in reaction engineering. The mean solids volume fraction and the mean solids velocity distribution are, of course, the primary variables of interest. Together, they determine the mean residence time of the solids in the riser. In this subsection, we focus the readers’ attention on the variance of the solids RTD, i.e., we present two alternative ways of estimating the solids-phase backmixing.

In multiple sojourns through the riser, i.e., the zone of interrogation of the scintillation detectors, the tracer particle traces out the trajectories of various solid particles. In other words, it samples various trajectory realizations that are possible in the solid phase under given operating conditions. A sample trajectory is shown in Figure 6. The trajectories during various tracer sojourns through the riser are of different lengths, in general, and because the instantaneous velocity fields seen by the tracer particle are different in each visit, the residence time spent in the riser during each visit is, in general, also different. It follows, therefore, that monitoring the distribution of residence times of the tracer particle in multiple visits (i.e., timing each trajectory of the tracer particle from the entrance to the exit of the riser) yields the residence time distribution of the entire phase. Indeed, interpreting the residence time distribution of the solid phase in this manner is completely compatible with the primitive definition of the residence time distribution $E(t)$ and is, in fact, the closest approximation to the true definition of residence time distribution (RTD).¹⁷ It is noteworthy that, because the riser behaves as a “closed” system, i.e., the tracer upon entry cannot leave through the entrance and upon departure at the top of the riser cannot re-enter, the RTD exists.

Figure 9 displays a histogram representing the RTD of the solid phase at $U_L = 20$ m/s and $S/L = 0.10$. For completeness, the total number of trajectories is re-

Table 2. Mixing Parameters from Solids RTD^a

S/L	solids mean residence time (s)	variance (s^2)	dimensionless variance	equivalent number of tanks in series	axial Peclet number
0.10	19.3	108	0.29	4	6.9
0.15	13.2	67.9	0.39	3	5.1
0.20	12.5	95.3	0.61	2	3.3

^a Liquid superficial velocity $U_L = 20$ cm/s.

ported, and the ordinate (frequency) is the fraction of trajectories that fall under a particular residence time “bin” of the histogram. All of the residence time distribution curves were found to be unimodal with an extended tail, indicating that the extent of backmixing in the solid phase is significant. Table 2 lists the mean residence time, the variance, and the dimensionless variance for the solid-phase RTDs obtained at different S/L ratios. Also listed are the parameters of a tanks-in-series and axial dispersion model that best describe the mixing pattern. Clearly, the backmixing in the solid phase is quite severe and increases with the solids-to-liquid flow ratio. Note that these *overall* backmixing parameters reflect backmixing both due to the *convective* velocity profile (which has a significant downflow fraction that increases with the liquid velocity and S/L ratio) and due to Lagrangian dispersion. It is also established that solids backmixing increases with increasing liquid velocity.⁷

It is noteworthy that, whereas the liquid was found to be essentially in plug flow, the solids phase exhibits severe backmixing. In the absence of solids, the high flow rate of liquid and the high L/D ratio of the riser would have ensured that the turbulent liquid flow is essentially in plug flow. The presence of solids naturally alters that pattern and introduces some degree of backmixing in the liquid. However, it is the solids, which enter from the side (eductor), as shown in Figure 2, and are *carried* by the liquid, that consequently suffer from severe backmixing. Liquid eddies interact with solid particles depending on the energy of the eddies and the inertia of the solid particles. For very small solid particles (micron size), the eddies capture the particles and carry them. For large solid particles, the eddies “slip” on them and, depending on their energies, can carry them some distance. What probably occurs in the liquid–solid riser, which has large (2.5-mm-diameter) particles that are denser (density = 2.5 g cm^{-3}) than the liquid (density = 1 g cm^{-3}), is that a typical energy-containing liquid eddy catches a particle and carries it upward for some distance, as long as it has sufficient energy. The energy dissipation mechanisms of liquid–solid, solid–solid, and solid–wall interactions and liquid turbulence extract energy from the eddy. Eventually, the solid particle can no longer be carried further upward and is “shed” by the eddy, which continues its journey to the exit of the riser. The particle falls downward, hitting other particles and eddies in the process, until it meets another eddy that has sufficient energy to carry it upward again. This mechanism continues until the particle finally finds its way out of the riser. Even such a simplified picture can explain why the solids suffer from severe backmixing whereas the liquid flows essentially in plug flow.

Although the RTD data discussed above provide very valuable information about global backmixing in the liquid–solid riser, such data include the effects of local solids dispersion *as well as* large-scale convective flow

of the solids. In addition to the global mixing of particles, the local mixing is equally important and affects to reactor performance, especially for fast reactions. It is useful to investigate, if possible, the local solids dispersion throughout the riser.

If one were to focus attention at any given point in the liquid–solid riser and release all of the solid particles from a given location at a given time, then, in subsequent time steps, the particles would disperse with the flow as they move outward in a random manner. Taylor¹⁸ showed that, if one were to monitor the motion of this “cloud” or “swarm” of particles, then the spread of this swarm would be related to the variance of particle positions at that time lag since their release. The theoretical arguments that lead to the evaluation of the components of the diffusivity tensor are involved and have been discussed in greater detail by Degaleesan¹⁶ and Roy.⁷ Here, we discuss the physical idea and present some of the key results in evaluating diffusivities from CARPT data.

In calculating diffusivities from CARPT data, we invoke the concept of ergodicity (that has been discussed earlier) to establish the equivalence of the Lagrangian motion of a single tracer particle over multiple trajectories through any cell to that of many particles released from that cell at the same time. At some time, if the tracer particle enters a computational cell (location in the column), a counter is turned on, and the particle is followed for about 200 subsequent steps. This kind of time scale has been found to be sufficiently large that the tracer particle “forgets” its history. When the particle returns again after a long time, a new trajectory tracking is initiated. This process is repeated for the entire data set over a large number of computational cells to collect sufficient statistics. The algorithm has been described in detail by Degaleesan.¹⁶ Thus, at the end of this process (after the entire data set has been treated), for each compartment, one has an ensemble of trajectories that originated in that compartment. Using ergodicity, this ensemble of trajectories can be viewed as a swarm of particles that were released at the same time from that compartment and eventually diffused out of the compartment.

Degaleesan¹⁶ showed that, in the presence of the radial gradient of net mean (z-directional) axial velocity, the axial diffusivity is given by

$$D_{zz}(\tau) = \int_0^\tau \left[\frac{\partial U_z}{\partial r} \right]_{z=r(\tau)} \left(\int_0^{\tau'} v_z'(\tau) v_r'(\tau') d\tau' \right) + \int_0^\tau v_z'(\tau') v_z'(\tau') d\tau' \quad (4a)$$

Correspondingly, the radial diffusivity (where there is no net flow in the radial direction) is given by

$$D_{rr}(\tau) = \int_0^\tau v_r'(\tau') v_r'(\tau') d\tau' \quad (4b)$$

Figure 10 displays the radial and axial diffusivities estimated using eqs 4 for the typical condition of $U_L = 20$ cm/s and $S/L = 0.15$. The diffusivities are plotted as functions of the time lag, because, in the general case, the rate of dispersion of the swarm of particles is a function of the time since the dispersion began. The radial dispersion is “quenched” by the presence of walls and is decreased to a much smaller value. The axial diffusivities grow freely to their asymptotic values at large times.

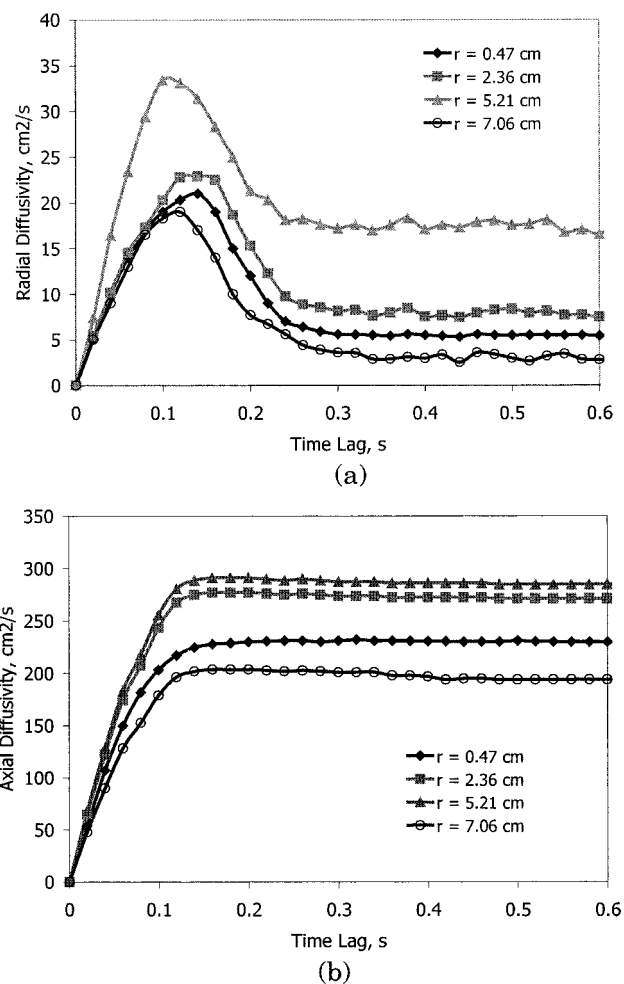


Figure 10. Solids diffusivities at selected radial locations. $U_L = 20$ cm/s; $S/L = 0.15$. (a) Radial, (b) axial.

Table 3. Axial and Radial Eddy Diffusivities and Axial Dispersion Coefficients (from Solids RTD)^a

S/L	D_{zz} (cm ² /s)	D_{rr} (cm ² /s)	D_{ax} (cm ² /s)
0.10	220	17.8	245
0.15	290	18.3	444
0.20	386	25.4	564

^a Liquid superficial velocity $U_L = 20$ cm/s.

By axial averaging of the above-determined asymptotic values of the radial and axial diffusivities between 75 and 150 cm of the riser, one can arrive at the radial profile of diffusivities that characterizes the local state of backmixing in the fully developed flow part of the riser. It is found that the radial diffusivity profile is relatively flat with values 1 order of magnitude lower than axial diffusivities.⁷ The axial diffusivity radial profiles exhibit a relatively flat maximum around r/R of about 0.6. Further averaging of the diffusivity profiles to arrive at a single number for characterization of the radial and axial eddy diffusion in the fully developed flow region of the riser leads to the values shown in Table 3 for $U_L = 20$ cm/s at three different solids loadings. Similar values are derived at other operating conditions. Increased solids-to-liquid flow ratios and increased liquid flow rates enhance the solids diffusivities. For comparison, the effective axial dispersion coefficients calculated from the variance of the solids RTDs measured by CARPT are also listed in Table 3. Note that the axial dispersion coefficients, D_{ax} , are

Table 4. Comparison of Characteristic Mixing Times^a

S/L solids/liquid flow ratio	characteristic solids convection time τ_c (s)	mean residence time from solids RTD (s)	characteristic axial diffusion time τ_D (s)	characteristic radial diffusion time τ_R (s)	Peclet number τ_D/τ_c	Peclet number for axial dispersion from RTD
0.10	19.1	19.3	148	13.3	7.7	6.9
0.15	13.4	13.2	112	13.0	8.3	5.1
0.20	12.6	12.5	83.9	9.3	6.7	3.3

^a Liquid superficial velocity $U_L = 20$ cm/s.

overall diffusivities that include the effects of the axial, radial, and aximuthal diffusivities, as well as the effect of the solids mean velocity profile. There is also the contribution from internal circulation at the entrance and exit of the riser, regions that have not been used (for lack of reliable data) in the diffusivity calculations reported in this section. Thus, these values of the effective axial overall diffusivities (i.e., axial dispersion coefficients) are consistently higher than the axial solids diffusivities, as they should be.

If one adopts the column diameter as the characteristic length scale for radial dispersion and the column length as the characteristic length scale for convection as well as axial dispersion (mixing), then one can estimate the characteristic times of the two processes. Table 4 reports the values for the two phenomena using the D_{zz} and D_{rr} values reported in Table 3. The mean residence times as well as the Peclet numbers calculated directly from the solids RTD are also listed for comparison. From Table 4, one observes that the characteristic convection times and the mean residence times from the RTD are in excellent agreement. The Peclet numbers based on the diffusivities are higher than those obtained from the solids RTDs. This is to be expected as the axial diffusivities are lower than the axial dispersion coefficient (Table 3). The RTDs contain that information on radial diffusion that contributes to axial dispersion and which is not accounted for in our simple comparison of convection and axial diffusion times. In addition, RTDs contain the effects of severe solids backmixing at the inlet of the riser and also at the exit, which is not accounted for in the τ_D/τ_c comparison that is developed only for the fully developed flow region of the riser.

3. Modeling

The preceding section indicates the extensive experimental characterization that is needed for the quantification of the solids flow pattern and backmixing in the riser. It is prohibitively costly to conduct such investigations at different scales of the riser and at all operating conditions that might be of interest. Therefore, the data described here and in Roy⁷ should be used to test the ability of appropriate fluid dynamic models to predict the observed solids holdup and velocity patterns. The model must be able to handle large-scale equipment to be of utility in industrial practice.

3.1. Governing Equations and Closures. In dispersed flows such as those existing within the liquid–solid riser under consideration, the precise way to model the flow field is (i) to solve the force balance (Newton's second law) on *each* particle in the system and trace the history of *each* particle from the point of entry until it leaves the system, (ii) to solve the momentum balance equation for the continuous liquid-phase incorporating the *coupling* between the dispersed and continuous phases, and (iii) to solve the elemental mass conservation equations for either phase. This is the so-called Euler–Lagrange approach,^{19–22} which has been suc-

cessfully adapted for some rather simple two-phase flows at low Reynolds' numbers. However, we note that the liquid–solid riser system has high liquid and solids fluxes, and at any typical condition, the total number of solid particles in the riser is over 900 000. Clearly, the resources required for solving a problem with two-way coupling between the phases (i.e., when motion of both the phases affect each other) are prohibitive, in terms of both the computational resource and the data storage requirements.

Consequently, in this study, we adopt the Eulerian two-fluid approach.^{23,24} In this approach, not only is the liquid-phase treated as a continuous phase, but the entire ensemble of solid particles is treated as a “pseudo-continuous” phase. Thus, one admits the existence of “two” *interpenetrating* fluids, i.e., both fluids are allowed to exist at the same point in space at the same time.²⁵ Following Drew,²⁵ the equations of continuity and motion are written for each phase as follows:

Continuity (k th phase)

$$\frac{\partial}{\partial t}(\epsilon_k \rho_k) + \nabla \cdot (\epsilon_k \rho_k \bar{\mathbf{u}}_k) = \sum_{p=1}^n m_{pk} \quad (5)$$

where $k = s$ for solids and $k = f$ for fluid

Momentum (fluid phase)

$$\frac{\partial}{\partial t}(\epsilon_f \rho_f \bar{\mathbf{u}}_f) + \nabla \cdot (\epsilon_f \rho_f \bar{\mathbf{u}}_f \otimes \bar{\mathbf{u}}_f) = -\epsilon_f \nabla p + \nabla \cdot \bar{\bar{\tau}}_f + \epsilon_f \rho_f \bar{\mathbf{g}} + K_{sf}(\bar{\mathbf{u}}_s - \bar{\mathbf{u}}_f) + \bar{\bar{F}}_f \quad (6a)$$

Momentum (solids phase)

$$\frac{\partial}{\partial t}(\epsilon_s \rho_s \bar{\mathbf{u}}_s) + \nabla \cdot (\epsilon_s \rho_s \bar{\mathbf{u}}_s \otimes \bar{\mathbf{u}}_s) = -\epsilon_s \nabla p - \nabla p_s + \nabla \cdot \bar{\bar{\tau}}_s + \epsilon_s \rho_s \bar{\mathbf{g}} + K_{sf}(\bar{\mathbf{u}}_f - \bar{\mathbf{u}}_s) + \bar{\bar{F}}_s \quad (6b)$$

Total volume conservation requires

$$\epsilon_s + \epsilon_f = 1 \quad (7)$$

Equation 5 represents the mass balance (continuity) of each phase. The left-hand-side terms represent the temporal and spatial gradients. The right-hand side represents the “mass creation” of the p th species (of n species) by reaction and is identically zero in our simulations because we do not consider any reactions. Equations 6a and 6b are momentum conservation equations for the liquid and solid phases, respectively. The left-hand side of each equation contains the transport terms, whereas the right-hand side contains the sources and sinks of momentum (forces). The hydrodynamic pressure is assumed to be shared by both phases, i.e., the flows of both the phases contribute to the pressure drop in the system. Hence, the gradient of pressure premultiplied by the respective volume fractions appear in both eqs 6a and 6b. In the case of solids

flow, collisions between individual solids particles contribute to both the normal stress (from the normal component of collisions) in the solids phase and the shear stress (arising from the tangential component of the momentum exchange in particle–particle collisions). These contribute to the solids-phase pressure p_s and shear stress term $\bar{\tau}_s$, respectively, the spatial gradients of which are the second and third terms on the right-hand side of eq 6b. The $\nabla \cdot \bar{\tau}_f$ term represents the liquid-phase stresses due to both the molecular and turbulent viscosity, and the $K_{sf}(\bar{u}_f - \bar{u}_s)$ terms represent the momentum exchange between the phases, through liquid–solid drag. Finally, eq 7 represents a constraint (definition of volume fraction) that must be satisfied everywhere in the computational domain and at all times, in that the total sum of volume fractions has to be identically unity.

In summary, eqs 5–7 express the following modes of momentum exchange (and transport of kinetic energy) between the liquid and solid phases: (1) interactions between particles and liquid resulting from the difference between their mean velocity fields, modeled as the drag force that drives the nonrandom part of the particle motion; (2) interactions within the particle velocity field between the mean and fluctuating components, which generate stresses in the particle assembly and give rise to solids-phase pressure and shear stress; (3) interactions between the mean velocity field of the liquid phase and the fluctuating liquid velocity, which give rise to the liquid-phase Reynolds stresses that dissipate the turbulent kinetic energy within the liquid phase; and (4) interactions between the particles with the fluctuating components of liquid velocity, which lead to particle diffusion in the liquid field and induce a flux of kinetic energy between the fluctuating velocities of the two phases. To complete the formulation of the model, we need to close the system of equations by expressing the various source and sink terms on the right-hand side of eq 6 in terms of the primitive velocity variables.

For modeling of the liquid–solid drag (i.e., momentum exchange between the mean solids velocity and the mean liquid velocity), we adopted the correlation of Wen and Yu.²⁶ This correlation was developed on the basis of studies with a broad set of experimental conditions. The expression for the drag coefficient reported by Wen and Yu²⁶ is

$$C_D = \frac{24}{\epsilon_f Re_p} [1 + 0.15(\epsilon_f Re_p)^{0.69}] \quad (8a)$$

The corresponding exchange coefficient²⁶ is

$$K_{sf} = \frac{18\mu_f}{d_p^2} \frac{\epsilon_s}{\epsilon_f^{2.7}} [1 + 0.15(\epsilon_f Re_p)^{0.69}] \quad (8b)$$

The solids flow in the riser is “compressible” (i.e., the solids volume fraction varies between 0.0 and the maximum packed volume fraction ϵ_{\max}), even though the solid material constituting the solid phase is practically incompressible. If the solids phase were to be viewed as a pseudo-continuous phase at the macroscopic scale (reactor scale), then clearly this phase responds to the local pressure field and undergoes deformation because the individual solid particles on the microscopic scale reconfigure depending on the local liquid and solids flow fields. We invoke this broad picture of the solid-phase behavior, analogous to the behavior of a gas, that has

led to the development of the *kinetic theory of granular solids*.^{27–32} This is a *phenomenological approach* used to render the collisional characteristics of the solids ensemble tractable within the two-fluid framework. Following the aforementioned authors, we define a *granular temperature* that is representative of the solid-phase fluctuations and transport properties³³

$$\theta_s = \frac{2}{3} k_s \quad (9)$$

where k_s is the kinetic energy due to solids velocity fluctuations. In this framework, it is possible to write a transport equation of the fluctuating kinetic energy of the solids phase, following Chapman and Cowling,³³ as

$$\frac{3}{2} \left[\frac{\partial}{\partial t} (\rho_s \epsilon_s \theta_s) + \nabla \cdot (\rho_s \epsilon_s \bar{u}_s \theta_s) \right] = (-p_s \bar{\mathbf{I}} + \bar{\mathbf{t}}_s) : \nabla \bar{u}_s + \nabla \cdot (k_{\theta_s} \nabla \theta_s) - \gamma_{\theta_s} + \phi_{fs} \quad (10)$$

In the above equation, θ_s is the granular pseudo-thermal temperature that represents the “fluctuating kinetic energy” in the solid phase. Each of the terms on the right-hand side of eq 10 have to be closed in terms of the granular temperature, in keeping with the basic philosophy of kinetic theory. In Table 5, we summarize the expressions used in the present simulations from the kinetic theory of granular solids.^{28–33} Note that the term γ_{θ_s} represents dissipation of the solids kinetic energy via collisions, and ϕ_{fs} represents the modulation of the solids kinetic energy by the liquid phase.

The liquid-phase turbulence was modeled using the standard $k-\epsilon$ model while accounting for the presence of the second (dispersed) phase.^{34,35} No-slip boundary conditions were used at the wall for the liquid (continuous) phase. However, the particles have a finite velocity at the wall. Thus, the suitable boundary conditions for the solids were chosen by assuming that the solids’ fluctuating kinetic energy is in local equilibrium at the wall. This implies that the sum of the flux of the granular temperature (i.e., the solids fluctuating kinetic energy flux) and the granular temperature generation at the wall (i.e., the source of fluctuating energy flux) is equal to the dissipation of fluctuating energy at the wall.³⁶ Mathematically, the balance of the production, transport, and dissipation of fluctuating energy flux at the wall is written as³⁶

$$q_{w,\theta_s} + \frac{\pi \rho_p u_s^2 \psi \sqrt{\theta_s}}{2\sqrt{3} \left(\frac{\epsilon_{s,\max}}{\epsilon_s} - \frac{\epsilon_{s,\max}}{\epsilon_s}^{2/3} \right)} - \frac{\sqrt{3} \pi \rho_p (1 - e_{sw}^2) \theta_s^{3/2}}{4 \left(\frac{\epsilon_{s,\max}}{\epsilon_s} - \frac{\epsilon_{s,\max}}{\epsilon_s}^{2/3} \right)} = 0 \quad (11)$$

3.2. Simulation Results. Note that the laboratory-scale riser on which the experimental data were collected is a three-dimensional unit in which the solids enter from the side through the solids eductor (Figure 2) and the liquid (water) enters from the bottom as well as from the side eductor. Consequently, there is a churning flow as the solids rise up in the riser, with significant azimuthal variation of the various instantaneous solids velocity components. The *instantaneous*

Table 5. Closures Used in CFD Model of the Riser^a

closure term	expression
solids pressure	$p_s = \rho_p \epsilon_s \theta + 2(1 + e_{ss}) \rho_p \theta g_0(\epsilon_s) \epsilon_s^2$
radial distribution function	$g_{0_{ss}} = \frac{1}{1 - \left(\frac{\epsilon_s}{\epsilon_{s_{\max}}}\right)^{1/3}}$
solids-phase shear viscosity	$\mu_s = \frac{4}{5} \epsilon_s \rho_s d_p g_{0_{ss}} (1 + e_{ss}) \left(\frac{\theta_s}{\pi}\right)^{1/2} + \frac{\epsilon_s \rho_s d_p \sqrt{\theta_s \pi}}{6(3 - e_{ss})} \left[1 + \frac{2}{5}(1 + e_{ss})(3e_{ss} - 1)\epsilon_s g_{0_{ss}}\right]$
solids conductivity	$k_s = \frac{150 \rho_s d_p \sqrt{\theta \pi}}{384(1 + e_{ss}) g_{0_{ss}}} \left[1 + \frac{6}{5} \epsilon_s g_{0_{ss}} (1 + e_{ss})\right]^2 + 2 \rho_s \epsilon_s^2 d_p (1 + e_{ss}) g_{0_{ss}} \sqrt{\frac{\theta_s}{\pi}}$
collisional dissipation term	$\gamma_{\theta_s} = \frac{12(1 - e_{ss}^2) g_{0_{ss}}}{d_p \sqrt{\pi}} \rho_s \epsilon_s^2 \theta_s^{3/2}$
energy dissipation due to interaction of solids and liquid fluctuations	$\phi_{sf} = -3K_{sf}\theta_s$

^a $\epsilon_{ss} = 0.98$; $\epsilon_{s,\max} = 0.6$.

flow field is clearly not axisymmetric (i.e., azimuthal variations are not negligible). However, as we have seen, the *time-averaged* axial solids holdup profile as well as the axial velocity profiles are approximately axisymmetric. This assumption is particularly true in the zone of “developed” flow in the riser, i.e., the zone in which the effects of the liquid distributor and the solids eductor are no longer important.

A full three-dimensional simulation of the riser necessitates huge computational resources to ensure a high enough resolution of the flow features. We recognize, however, that we are first interested in testing the CFD models against the time-averaged data and determining whether the microscopic models adopted for the simulation are able to provide reasonable quantitative predictions of the observed macroscopic flow quantities. To achieve this, it seemed expedient to assume axisymmetry in the flow simulation. This assumption makes the simulation much less computationally demanding and tractable within finite time and is expected to capture the time-averaged flow field with fidelity.

The above-described two-fluid model was implemented in the FLUENT framework. The numerical simulations were performed on a 192 (axial) \times 8 (radial) rectangular grid, thus involving a total of 1536 computational cells. The aspect ratio of each cell was close to 1.0. Equations 5–7 were solved, with inputs from the appropriate closure forms, in a transient fashion with a time step of 0.001 s. The time step was relaxed successively to 0.01 s as the final steady-state profile was approached. Within each time step, the conservation equations were solved through a number of subiterations between the momentum and the continuity equations. Iterations were continued until continuity was satisfied with a residual error of less than 10^{-3} in the pressure variable (for other variables, the accuracy was better). It took approximately 40–50 iterations per time step to ensure this kind of convergence. The under-relaxation parameters for the solution scheme were set to 0.6 for the pressure and 0.4 for the velocities.

At the inlet, the boundary conditions were set so as to impose a uniform solids–liquid distribution, and the overall flow rates of the solids and liquid were set to the solids flow rate measured at the eductor (Figure 2). All flow of energy was assumed to be limited to the mean flow. The outlet boundary conditions were purely

convective, i.e., they ensure overall mass conservation of each of the phases in the riser. Symmetry conditions were imposed at the central axis of the column. The boundary conditions at the wall were as discussed above. All simulations were performed by assuming the solids–solids and solids–wall restitution coefficient to be 0.98. Sensitivity to this parameter was examined,⁷ and the predicted profiles were not found to be highly sensitive in the vicinity of 1.0 (i.e., e_{ss} in the range 0.95–1.0).

The computed solids velocity vectors indicated solids rising in the middle and downflow by the walls, in qualitative agreement with experimentally observed flow patterns of Figure 7. The computed solids accumulation at the bottom of the riser, which is expected, and the radial solids holdup profile, which is invariant with axial position in the main body of the riser, are in line with experimental observations. This profile is qualitatively similar to the CT findings presented in Figure 3. It is worth noting here that imposition of the symmetry boundary condition at $r = 0$ causes the flow to develop quickly (around the first 5 s of real time) and reach its long-time pattern. In contrast, the real experiment is characterized by a highly dynamic flow, with three-dimensional vortical particle swarms and liquid vortices moving in a complex fashion and often crossing the centerline axis. In the simulation, by imposing the symmetry condition on the axis, the possibility of that such structures would form and would cross the axis of symmetry is ruled out, and the flow is forced to follow and develop into its time-averaged solution. Thus, further time-averaging at large times does not alter the stationary pattern that is developed. In this sense, a transient *axisymmetric* simulation is similar to a steady-state simulation in which the flow is *assumed* to be time-invariant.

In Figure 11a, the computed time-averaged solids axial velocity profile is compared to the time-averaged velocity profiles obtained by CARPT. Clearly, the agreement of velocity profiles is quite good. The agreement was found to be similar and satisfactory at other operating conditions. In Figure 11b, the comparison of the time-averaged solids radial holdup is presented against the axially averaged time-averaged solids holdup profile measured via CT. The prediction is reasonable, although the simulated profile tends to overpredict the

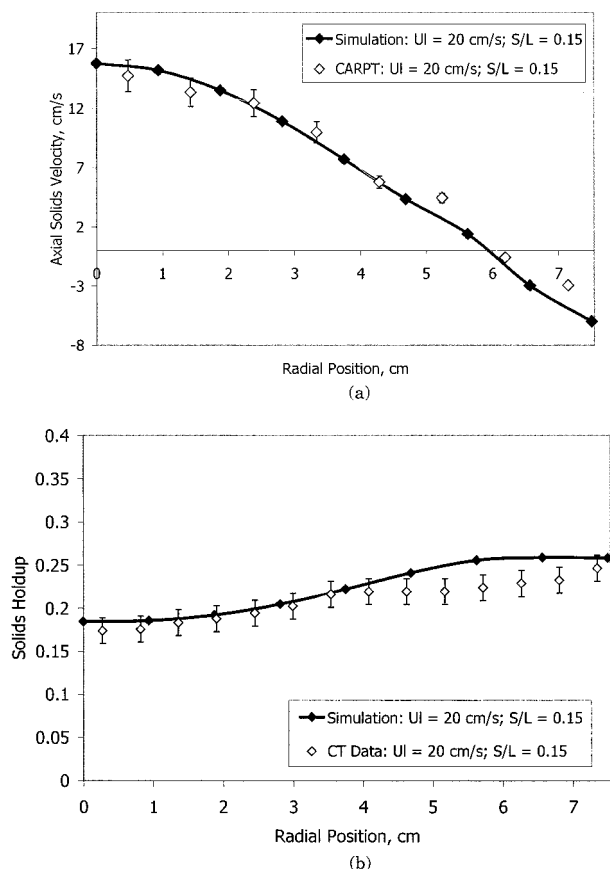


Figure 11. (a) Comparison of simulated solids velocity profile compared to axially averaged time-averaged solids axial velocity data measured via CARPT. (b) Comparison of simulated solids holdup profile compared to axially averaged time-averaged solids holdup data measured via CT.

solids holdup at the walls. It is difficult to isolate why this occurs, but possibly the most important reason for this discrepancy is that the inlet conditions are not modeled accurately in the two-dimensional axisymmetric model. In the real experiment, there is a significant loss in flow energy at the distributor and at the eductor. Hence, the actual liquid flow rate is able to support a smaller solids flow rate into the developed zone of the riser. In the simulation, this has not been accounted for explicitly; hence, the liquid has more energy available to drag the solids with it. Yet, by imposing the overall mass balance, the *net* flow allowed through the riser is the same as that found in the experiments (through the inlet and outlet boundary conditions). The only way this could be reconciled is by allowing a slightly greater net downflow rate at the wall in the simulation, which is possible if the radial segregation of solids is higher in the simulation.

Having established the two-dimensional flow field and validated the simulation results against CARPT-CT data, the next step was to determine whether the global backmixing could be estimated with the CFD simulation. Because the simulation reaches a stationary invariant state, the final steady-state field was utilized for the calculation. Nonreacting scalars (tracers) were tagged to each of the phases and introduced at the inlet boundary of the flow field. The momentum calculations were turned off, and the scalars were allowed to distribute in the stationary-state flow field. The net result of such a calculation is that one is able to recover the residence time distributions (RTDs) of the phases.

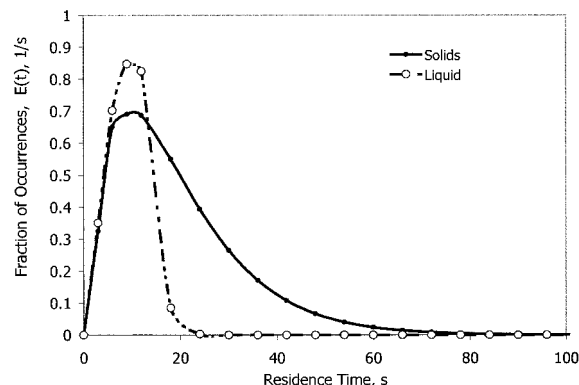


Figure 12. Solids and liquid RTDs calculated from solution of the scalar transport equation for $U_L = 20$ cm/s and $S/L = 0.15$.

Note that, because only the final stationary-state flow field has been used, this is equivalent to completely ignoring the micromixing effects (terms of the kind $\langle u'_i C' \rangle$ are ignored in the scalar transport equation).

The concentration of tracer is monitored at the exit and is “flow-averaged” to yield the “mixing cup” concentration of tracer. The flow-averaged tracer concentration is given by

$$\langle C \rangle_{\text{flow}} = \frac{\int_0^R 2\pi r r \epsilon(r) u_z(r) C(r) dr}{\int_0^R 2\pi r r \epsilon(r) u_z(r) dr} \quad (12)$$

The equation is valid for *each* phase provided the appropriate phase holdup and velocity are used. The evaluation of eq 12 is made at each time step so that the outlet mixing cup concentration as a function of time is recovered. Note that, because a dimensionless scalar (tracer) concentration of unity was imposed at the inlet, the tracer response curve at the outlet is equivalent to the RTD (E curve) for each phase.

Figure 12 shows a typical set of RTD curves for the solids and liquid evaluated from solving the scalar transport equations for each phase at $U_L = 20$ cm/s and $S/L = 0.15$. Clearly, the liquid flow pattern is much closer to plug flow than that of the solids, as also found experimentally. Moreover, the dimensionless variance of the solids RTD is 0.41, which is in excellent agreement with the value of 0.39 (Table 2) obtained experimentally. This is additional evidence that the 2D axisymmetric simulation of the liquid–solid flows in the riser is capable of providing the needed information for reactor design.

For example, curves of the type plotted in Figure 12, or in the moments, can be used as inputs to reactor models. Instead of evaluating RTD curves characteristic of reactor vessels at selected operating conditions by actual experiment, we can compute them as shown here. Often, reaction kinetics is complex and consists of multiple steps, so that a complete solution of the fluid mechanics, mass transfer, and kinetics using CFD techniques becomes prohibitive. In such situations, it is instructive to *decouple* the flow and reaction problems by following a procedure elucidated in this section. The individual phase tracer curves for the phases can be evaluated by CFD, as this problem is computationally less severe. The moments of these distributions reflect the phase backmixing and can be implemented to make reactor-scale predictions. Such a scheme has also been

implemented recently in the modeling of *n*-butane partial oxidation in a gas–solids riser.³⁷

4. Summary and Conclusions

This paper summarizes some key findings from a doctoral thesis on liquid–solids risers.⁷ As a result of this work, we now know that the cross-sectional solids distribution is not totally uniform and that there is a slight increase in the solids concentration at the wall. The solids holdup *distribution* as a function of liquid velocity and solids flux is now available. We have firm evidence for the time-averaged solids velocity, which exhibits a clear pattern even though the instantaneous solids velocity field is highly turbulent and chaotic. In the time-averaged sense, the solids rise in the middle of the riser and flow downward by the wall. We have also concluded that, even though the liquid can be assumed to be in plug flow, the solids are severely backmixed. This could be an important consideration for reactor performance predictions. The extent of solids backmixing depends on the solids loading (increases with increased loading) and on the liquid flow rate (increases with increased flow rate).

The CFD two-fluid simulation provided a qualitative and quantitative picture of what happens at the microscale in the riser and how it affects the overall flow patterns. Comparisons of the predicted solids velocity profiles and solids holdup profile as well as of the computed solids and liquid RTDs with the available experimental data are good. This implies that the developed CFD model can be used for scale-up and design. With rapid advancements in computational power, the design engineer should soon be able to use these models for actual design and troubleshooting at real industrial-scale reactors. Until that becomes a reality, the CFD models (which have been quantitatively validated as well on a laboratory-scale unit) can still provide useful insights into flow patterns and phase distributions. They can also be used to predict tracer RTD curves, as shown in this paper, which, in turn, can be used to generate inputs for phenomenological reactor models.

Acknowledgment

Both authors are grateful for the industrial support from CREL sponsors that made this work possible and for the assistance of Dr. A. Kemoun and Prof. M. H. Al-Dahhan in planning and executing portions of this study.

Nomenclature

d_p = particle diameter, m
 c = constant in eq 1
 C = concentration of simulated tracer, mol m⁻³
 C_D = drag coefficient
 D = diffusivity, m² s⁻¹
 e_{ss} = coefficient of restitution between solid particles
 e_{sw} = coefficient of restitution between solid particles and wall
 F = body force, N
 g = acceleration due to gravity, m s⁻²
 g_{0ss} = solids radial distribution function
 k_s = kinetic energy per unit mass of solids, m² s⁻²
 $k_{\theta s}$ = coefficient of granular conductivity, kg m⁻¹ s⁻¹
 K_{st} = momentum exchange coefficient, kg m³ s⁻¹
 m = constant in eq 1

n = constant in eq 2
 p = pressure, N m⁻²
 p_s = solids pressure, N m⁻²
 r = radial coordinate, m
 q_s = granular kinetic energy flux, kg s⁻³
 Q_s = solids flow rate, m³ s⁻¹
 R = radius of tube/vessel, m
 Re_p = Reynolds number based on particle diameter
 S/L = solids-to-liquid flow ratio
 \bar{u}_k = velocity vector of phase k , m s⁻¹
 U = local liquid velocity, m s⁻¹
 U_L = liquid superficial velocity, m s⁻¹
 t = time, s
 v_r = radial component of the solids (particle) velocity, m s⁻¹
 v_θ = azimuthal component of the solids (particle) velocity, m s⁻¹
 v_z = axial component of the solids (particle) velocity, m s⁻¹
 $v_z(0)$ = centerline axial solids (particle) velocity (eqs 4 and 5), m s⁻¹
 v_{zi} = mean axial velocity of tracer particle in the i th trajectory, m s⁻¹
 x = spatial coordinate, m
 y = spatial coordinate, m
 z = axial coordinate, m

Greek Symbols

α_1 = constant in eq 2
 α_2 = constant in eq 2
 $\gamma_{\theta s}$ = collisional dissipation term (eq 10), kg m⁻¹ s⁻³
 ϵ_k = volume fraction (holdup) of phase k (eq 5)
 ϵ_s = solids volume fraction (holdup)
 ϵ'_s = deviation in solids volume fraction (holdup) from mean
 ϵ_{sA} = cross-sectionally averaged solids holdup
 ϕ_{sf} = term modeling solids energy dissipation by correlations between solids and liquid velocity fluctuations (eq 10), kg m⁻¹ s⁻³
 μ_s = solids viscosity (eq 10), kg m⁻¹ s⁻¹
 μ_f = molecular viscosity of the fluid, kg m⁻¹ s⁻¹
 ρ_f = fluid density, kg m⁻³
 ρ_s = solids density, kg m⁻³
 q = azimuthal coordinate, radian
 θ_s = granular temperature, m² s⁻²
 σ^2 = variance of RTD, s²
 σ_D^2 = dimensionless variance of RTD, s²
 σ_ϵ = standard deviation of cross-sectionally averaged solids holdup
 τ' = time lag, s
 $\bar{\tau}_s$ = stress in the solids, N m⁻²

Literature Cited

- (1) Villiermaux, J. Future Challenges for Basic Research in Chemical Engineering. *Chem. Eng. Sci.* **1993**, *48*, 2525.
- (2) Krishna, R.; Sie, S. T. Strategies for Multiphase Reactor Selection. *Chem. Eng. Sci.* **1994**, *49* (24A), 4029.
- (3) Lerou, J. J.; Ng, K. M. Chemical Reaction Engineering: A Multiscale Approach to a Multiobjective Task. *Chem. Eng. Sci.* **1996**, *51*, 1595.
- (4) Dudukovic, M. P.; Larachi, F.; Mills, P. L. Multiphase Reactors—Revisited. *Chem. Eng. Sci.* **1999**, *54*, 1975.
- (5) Corma, A.; Martinez, A. Chemistry, Catalysts and Processes for Isoparaffin Alkylation: Actual Situation and Future Trends. *Catal. Rev.—Sci. Eng.* **1993**, *35* (4), 483.
- (6) Vora, B.; Pujado, P.; Imai, T.; Fritsch, T. Production of Detergent Olefins and Linear Alkylbenzenes. *Chem. Ind.* **1990**, *6*, 187.
- (7) Roy, S. Quantification of Two-Phase Flows in Liquid–Solid Risers. D.Sc. Dissertation, Washington University, St. Louis, MO, 2000.
- (8) Thomas, C. L. *Catalytic Processes and Proven Catalysts*; Academic Press: New York, 1970.

- (9) Edmonds, T. Oil Based Chemistry. In *Catalyst and Chemical Processes*; Pearce, R., Patterson, W. R., Eds.; John Wiley and Sons: New York, 1981.
- (10) Weitkamp, J. In *Catalysis by Zeolites*; Imelik B., Naccache, C., Bentaaret, Y., Vedrene, J. C., Goudurier, G., Prailand, H., Eds.; Elsevier: Amsterdam, 1980, pp 65–76.
- (11) Roy, S.; Kemoun, A.; Al-Dahhan, M. H.; Dudukovic, M. P. A Method for Estimating the Solids Circulation in a Closed-Loop Circulating Fluidized Bed. *Powder Technol.* **2001**, in press.
- (12) Kumar, S. B. Computed Tomography Measurements of Void Fraction and Modeling of Flow in Bubble Columns. Ph.D. Dissertation, Florida Atlantic University, Boca Raton, FL, 1994.
- (13) Kumar, S.; Moslemian, D.; Dudukovic, M. P. A Gamma Ray Tomographic Scanner for Imaging Void Fraction Distribution in Bubble Columns. *Flow Meas. Instrum.* **1995**, *6* (11), 61.
- (14) Devanathan, N. Investigation of Liquid Hydrodynamics in Bubble Columns via Computer Automated Radioactive Particle Tracking (CARPT). D. Sc. Thesis, Washington University, St. Louis, MO, 1991.
- (15) Larachi, F.; Kennedy, G.; Chaouki, J. 3-D Mapping of Solids Flow Fields in Multiphase Reactors with RPT. *AIChE J.* **1995**, *41*, 439.
- (16) Degaleesan, S. Fluid Dynamic Measurements and Modeling of Liquid Mixing in Bubble Columns. D.Sc. Thesis, Washington University, St. Louis, MO, 1997.
- (17) Nauman, E. B.; Buffham, B. A. *Mixing in Continuous Flow Systems*; John Wiley and Sons: New York, 1983.
- (18) Taylor, G. I. Diffusion by Continuous Movements. *Proc. London Math. Soc.* **1921**, *20*, 196.
- (19) Joseph, D. D.; Hu, H.; Crochet, M. Direct Numerical Simulation of Fluid-Particle Motions. *J. Theor. Comput. Fluid Dyn.* **1992**, *3*, 285.
- (20) Pan, Y.; Banerjee, S. Numerical Simulation of Particle Interactions with Wall Turbulence. *Phys. Fluids* **1996**, *8*, 2733.
- (21) Pan, Y.; Banerjee, S. Numerical Investigation of the Effects of Large Particles on Wall Turbulence. *Phys. Fluids* **1997**, *9*, 3786.
- (22) Delnoij, E.; Kuipers, J. A. M.; van Swaaij, W. P. M. Computational Fluid Dynamics applied to Gas–Liquid Contactors. *Chem. Eng. Sci.* **1997**, *52* (21/22), 3623.
- (23) Anderson, T. B.; Jackson, R. A Fluid-Mechanical Description of Fluidized Beds. *Ind. Eng. Chem. Fundam.* **1967**, *6*, 527.
- (24) Harlow, F. H.; Amsden, A. A. Numerical Calculation of Multiphase Fluid Flow. *J. Comput. Phys.* **1975**, *17* (1), 19.
- (25) Drew, D. A. Mathematical Modeling of Two-Phase Flow. *Annu. Rev. Fluid Mech.* **1983**, *15*, 261.
- (26) Wen, C. Y.; Yu, Y. H. Mechanics of Fluidization. *Chem. Eng. Prog. Symp. Ser.* **1966**, *62* (62), 100.
- (27) Bagnold, R. A. Experiments on a Gravity-Free Dispersion of Large Solid Spheres in a Newtonian Fluid under Shear. *Proc. R. Soc. London* **1954**, *A225*, 49.
- (28) Savage, S. B.; Jeffrey, D. J. The Stress Tensor in a Granular Flow at High Shear Rate. *J. Fluid Mech.* **1981**, *140*, 255.
- (29) Jenkins, J. T.; Savage, S. B. A Theory for the Rapid Flow of Identical, Smooth, Nearly Elastic Spherical Particles. *J. Fluid Mech.* **1983**, *130*, 187.
- (30) Lun, C. K. K.; Savage, S. B.; Jeffrey, D. J.; Chepuriniy, N. Kinetic Theories for Granular Flow: Inelastic Particles in Couette Flow and Slightly Inelastic Particles in a General Flow Field. *J. Fluid Mech.* **1984**, *140*, 223.
- (31) Sinclair, J. L.; Jackson, R. Gas-Particle Flow in a Vertical Pipe with Particle–Particle Interactions. *AIChE J.* **1989**, *35*, 1473.
- (32) Ding, J.; Gidaspow, D. A Bubbling Fluidization Model Using Kinetic Theory of Granular Flow. *AIChE J.* **1990**, *36*, 523.
- (33) Chapman, S.; Cowling, T. G. *Mathematical Theory of Non-Uniform Gases*, 3rd ed.; Cambridge University Press: Cambridge, U.K., 1990.
- (34) Launder, B. E.; Spalding, D. B. The Numerical Computation of Turbulent Flows. *Comput. Methods Appl. Mech. Eng.* **1974**, *3*, 269.
- (35) Elghobashi, S. E.; Abou-Arab, T. W. A Two-Equation Turbulence Model for Two-Phase Flows. *Phys. Fluids* **1983**, *26* (4), 931.
- (36) Johnson, P. C.; Jackson, R. Frictional–Collisional Constitutive Relations for Granular Materials with Application to Plane Shearing, Sheared in an Annular Cell. *J. Fluid Mech.* **1987**, *176*, 67.
- (37) Roy, S.; Dudukovic, M. P.; Mills, P. L. A Two-Phase Compartments Model for the Selective Oxidation of *n*-Butane in a Circulating Fluidized Bed Reactor. *Catal. Today* **2000**, *61*, 73.

Received for review February 26, 2001
 Revised manuscript received June 25, 2001
 Accepted June 27, 2001

IE010181T